VENUS: a comprehensive electro-thermo-opto VCSEL simulator

VENUS: a comprehensive electro-thermo-opto VCSEL simulator

Alberto Tibaldi[a,b], Francesco Bertazzi[a,b], Michele Goano[a,b], Markus Daubenschüz[c], Rainer Michalzik[d], and Pierluigi Debernardi[a]

[a]Istituto di Elettronica e di Ingegneria dell'Informazione e delle Telecomunicazioni (IEIIT), Consiglio Nazionale delle Ricerche (CNR), c/o Politecnico di Torino, Corso Duca degli Abruzzi 24, 10129 Torino (TO), Italia

[b]Dipartimento di Elettronica e Telecomunicazioni, Politecnico di Torino, Corso Duca degli Abruzzi 24, 10129 Torino (TO), Italia

[c]Philips Photonics GmbH, Lise-Meitner-Straße 13, 89081 Ulm, Germany

[d]Institute of Functional Nanosystems, Ulm University, Albert-Einstein-Allee 45, 89081 Ulm, Germany

ABSTRACT

The operation of vertical-cavity surface-emitting lasers (VCSELs) results from the interplay among different physical mechanisms. For this reason, even a basic VCSEL model must address the coupling of electrical injection, stimulated/spontaneous emission and optical resonances, without disregarding the strong thermal effects affecting each of these models, leading to the need of an entangled multiphysical description. With the aim to fill the present gap of advanced comprehensive VCSEL models, in this work we present our VCSEL electro-opto-thermal numerical simulator (VENUS). The paper describes the VENUS constitutive blocks and their coupling strategy. The model is then validated by comparing the most significant lasing features with experimental results.

Keywords: VCSELs, numerical device simulation, multiphysics simulation, electro-thermo-optical device model

1. INTRODUCTION

VCSELs are consolidating their starring role in the mass market of semiconductor light sources. After being key components in optical mice, sensors and datacom systems for their inexpensiveness, low power consumption and reliability,[1] they are becoming the enabling devices in 3D cameras or time-of-flight sensors for automotive and smartphone pervasive applications.[2,3] In such contexts, CAD tools represent the best possible support to VCSEL engineers to minimize the design costs.

VCSEL modeling is a complex task, as it requires accurate descriptions of optical, electrical, and thermal phenomena, and of their entangled interplay. Although few commercial codes can simulate standard structures, at present they cannot handle polarization-stabilized VCSELs (by gratings or other anisotropies), which are required in several innovative applications. In an effort to progress in this field, in this work we present our in-house VCSEL electro-opto-thermal numerical simulator VENUS.[4] VENUS features four building blocks: the 3D vectorial vcsel electromagnetic (VELM) code,[5,6] which is a numerically efficient optical solver based on a modal expansion technique, widely tested with other solvers and with experimental results.[7–15] The stimulated and spontaneous emission of quantum well active regions are evaluated within a many-body description,[16] with the sub-bands calculated by a 4-band $\mathbf{k}\cdot\mathbf{p}$ perturbation approach.[17–20] The thermal problem is solved by an ad-hoc spectral element method.[21] Finally, carrier transport is based on a drift-diffusion model,[16,22–24] augmented with

Further author information: (Send correspondence to Alberto Tibaldi)
Alberto Tibaldi: E-mail: alberto,tibaldi@polito.it, Telephone: +39 011 090 5437
Pierluigi Debernardi: E-mail: pierluigi.debernardi@ieiit.cnr.it, Telephone: +39 011 090 5420

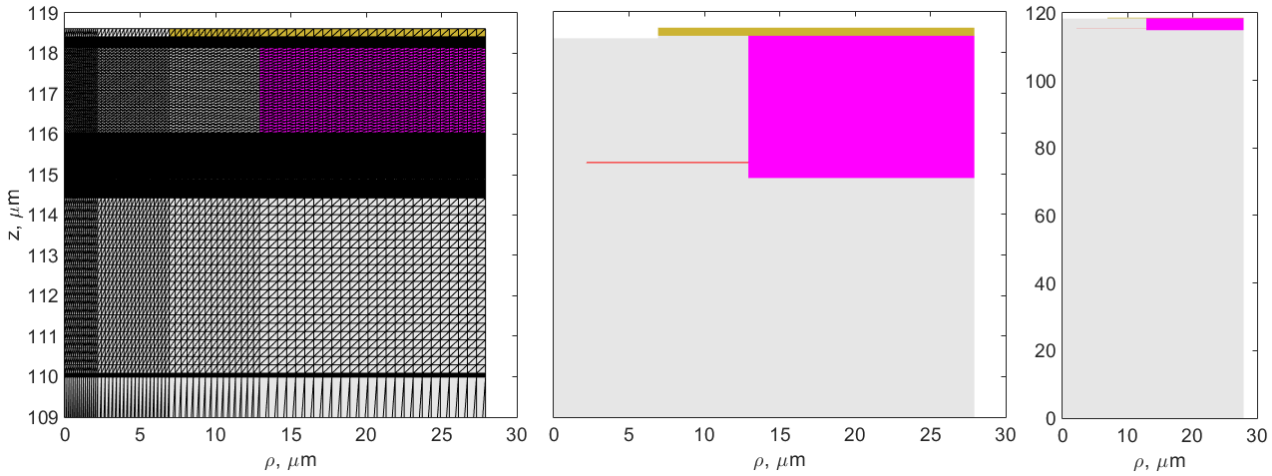

Figure 1. Device cross-section, limited to the drift-diffusion computational window, illustrating the main transverse features of the device under analysis. Left: mesh of the electrical solver, longitudinally zoomed into the VCSEL section. Center: same as left, without showing the meshing (see text for the description of the different regions). Right: the whole simulated geometry, including also the 110 μm thick substrate.

quantum corrections to better describe the active region and with photon rate equations to allow coupling with the optical model.[16,25–28]

The VENUS simulation capabilities are demonstrated through detailed comparisons with experimental results obtained on a device produced and characterized by Philips Photonics. To this aim, the discussion is focused on the different physical mechanisms behind the prediction of the transverse mode competition, which is validated by wavelength- and current-resolved measurements.

2. MULTISCALE, MULTIPHYSICS VCSEL SIMULATION RESULTS

To show the features of VENUS and investigate some aspects of VCSEL operation such as mode competition, we select a specific device and we fully characterize it, both numerically and experimentally. We use an oxide-confined AlGaAs VCSEL with the following main characteristics: the 1λ-cavity features three 8 nm GaAs QWs, placed at the maximum of the optical standing wave. The 30 nm oxide layer is placed in the first of the 21 pairs of the p-DBR outcoupling mirror. The corresponding 4 μm oxide aperture at the device axis provides both current and optical confinements; the bottom DBR includes 37 pairs. Both mirrors are subjected to composition and doping gradings to optimize the conduction features and, at the same time, to keep the free-carrier absorption losses at a minimum.

Several devices from the same chip have been processed in arrays, featuring rows with the same nominal oxide aperture and columns with different apertures, ranging from 1 to 10 μm. For this paper, we selected a device with a small size, to keep the presentation of the mode competition as simple as possible. In the experimental campaign, the heatsink temperature was varied by a Peltier element set to temperatures of 20, 50, 80, and 110 °C. The results presented here refer to 50 °C operation to address an intermediate temperature among those available from the experiments.

After an extensive parameter tuning campaign we achieved a satisfactory agreement between model and experiment over the whole range of temperature and sizes. A detailed discussion of the most important parameters (here just provided in Appendix A) and of the model performance as a function of temperature and size is delayed to a future publication. Here we focus on the specific case previously described, whose cross-section is shown in Fig. 1.

The VCSEL is grown on an n-doped GaAs substrate that is later thinned to 110 μm. In the VCSEL volume the mesh is longitudinally denser, as can be appreciated from the figure, where just a portion of the substrate domain is visible (a 3 μm longitudinal discretization is applied there). In particular, one can notice the two regions

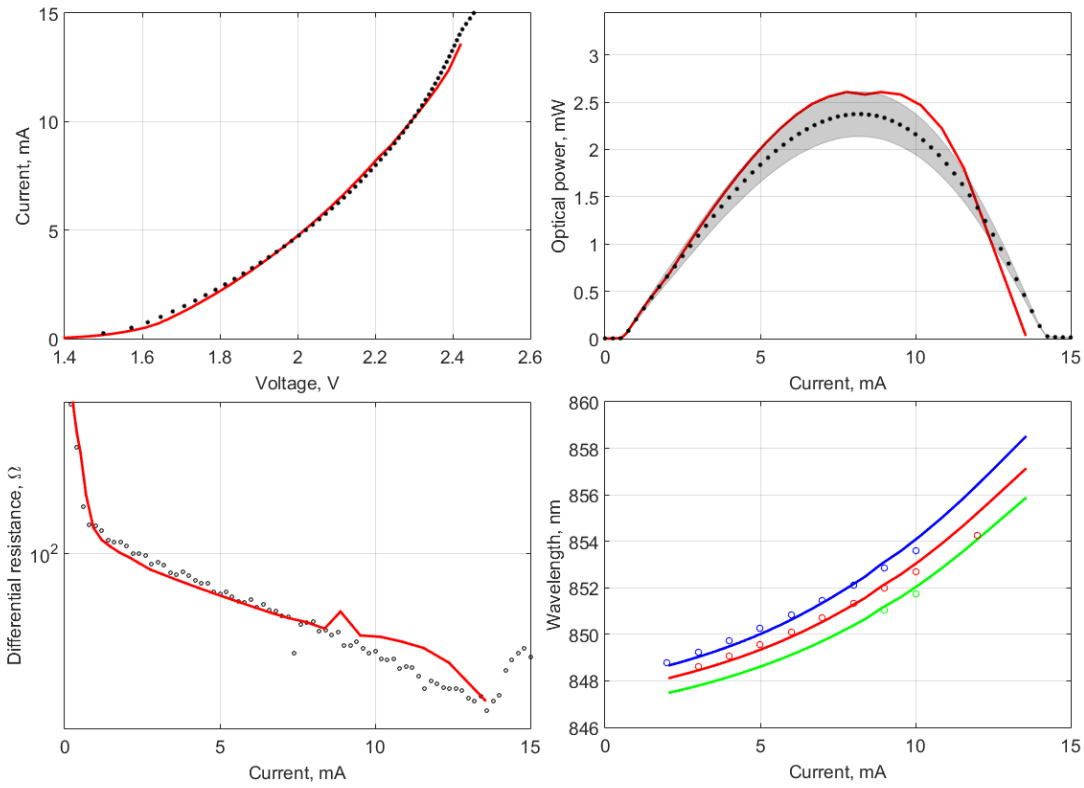

Figure 2. VENUS output chart for the 4 μm oxide aperture device under investigation, at 50 °C. The chart features from left to right, top to bottom: IV characteristics, LI characteristics, differential resistance, and modal wavelengths. The experimental results are indicated by dots or open circles, VENUS outputs with continuous lines.

of the n- and p-DBRs, which are approximated by an average material only for the drift-diffusion and thermal solvers.[29] This simplified approach leads to 27496 mesh nodes (76 radial and 365 longitudinal points). It is to be remarked that the number of equations (including Poisson's and electron/hole continuity equations) is roughly threefold the number of nodes. We have verified that a full simulation with the exact material composition introduces just minor differences, but allows much faster computations. Only the drift-diffusion solver relies on an extensive spatial discretization, whereas both thermal and optical solvers are based on modal expansions. For this reason no grid adaptation is required at all, reducing the multiphysics couplings to the simple evaluation of the optical and thermal quantities on the drift-diffusion mesh points.

The VCSEL features a mesa of about 13 μm radius (see Fig. 1, center) to apply the oxidation of the exposed quasi-AlAs layer. After the oxidation process, a passivation layer (indicated in magenta) is deposited to insulate the mesa sides and reduce the parasitic capacitance. The current is then injected through the 6 μm radius metal ring in contact with the top GaAs layer, where an ohmic contact is obtained by a p^{++}-metal junction. Notice that the electrical domain comprises the whole mesa and extends more than twice in the radial direction (see Fig. 1). This is an optimized solution domain that was determined by increasing the boundary until the solutions did not change any longer. In the passivation and oxide regions the current continuity equations are disabled (only Poisson's equation is solved) to enforce insulating conditions.

In Fig. 2 the main outputs provided by VENUS are presented. In this output chart, all the experimental results (dots or circles) are superimposed to the numerical data. It can be observed that the overall features are nicely reproduced. In particular, the current-voltage (IV) curve and corresponding differential resistance match very well with the measurements.

The total optical output power versus current (LI) characteristics, taking into account the experimental

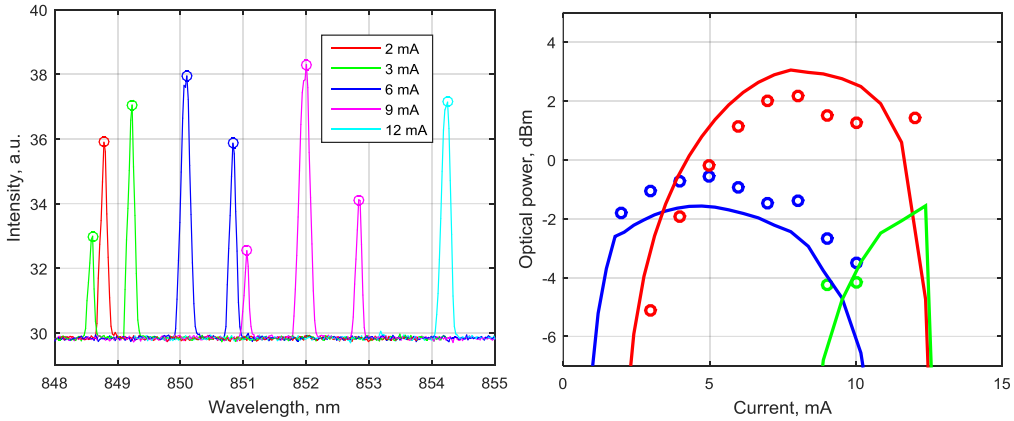

Figure 3. Measured spectra versus current (left); the peak powers (dots) are rescaled to the total power in Fig. 2 and plotted as dots in the right plot, allowing a direct comparison with the VENUS simulation.

uncertainties in the shaded region, is likewise well reproduced, hits the slope efficiency, and excellently predicts the power rollover current. The very good alignment of experimental and measured wavelengths (see comments to Fig. 3 below) indicates a fair treatment of the thermal problem that rules the the VCSEL power rollover.

With a 4 μm oxide aperture, the VCSEL operation is basically bimodal: fundamental and first higher-order modes. This can be investigated in detail thanks to the optical spectra measured at different injection currents, as shown in Fig. 3. This is very important for our comparisons, where the only way to keep track of the temperature rise in the devices is through the wavelength red-shift. The highest value of the optical spectra is the included power modal information, disclosing which transverse mode is lasing and in which proportion to the other ones.[30] Therefore, in the right plot of Fig. 3 the mode peak heights (LP_{01}, LP_{11}, and LP_{02} in blue, red, and green, respectively) are reported versus current, where a fair agreement with the experiments can be observed.

The devices under investigation show a good circularity and low birefringence, so no particular feature show up, unlike, *e.g.* in 8. The good circularity can be well grasped from the spectra of Fig. 3(left), where one can barely see some faint signatures of double peaks at the first-order mode. Therefore VENUS, which at present treats the transport of axisymmetric structures, can be safely applied. Polarization features, natively included in VELM, are not investigated in this work due to the lack of experimental results.

The most important parameter influencing transverse mode competition is carrier diffusion in the QWs. In fact, the mode competition is governed by spatial hole-burning, which distributes gain differently to each transverse mode at increasing optical power. The spatial hole is dug according to the modal field intensity profiles at the longitudinal QW positions. The depth of such a spatial hole in the gain profile depends on the carrier diffusion and is drastically different for electrons and holes. Carrier mobilities have been investigated and characterized in depth for bulk GaAs.[31,32] Besides alloy composition, they vary with doping[33] and temperature, which might play a relevant role in this devices, where the maximum internal temperature increase is of the order of 250 °C. In the present paper we assume QW mobilities that are six times smaller than bulk values, which can be ascribed to well-barrier interface roughness.[34]

Finally, in Fig. 4 we show the effect of increasing the current on three important internal (not experimentally observable) quantities ruling VCSEL operation and mode competition: 2D carrier densities (left), temperature (center), and modal intensity profiles (right). This figure also highlights the different simulation domains of the VENUS constituents, tailored according to the corresponding physics. For instance, the QW carrier densities are defined within the whole mesa, up to the passivation.

The temperature profile is computed in the entire device volume ($z \times \rho = 120 \times 150\,\mu m^2$) and is reported here only in the electrical domain. The temperature kink at the mesa boundary marks the strong difference in the thermal conductivity between semiconductor and passivation. The mode profile plot on the right emphasizes the strong impact of thermal guiding. Focusing for example on the fundamental mode (red), a sharp squeezing

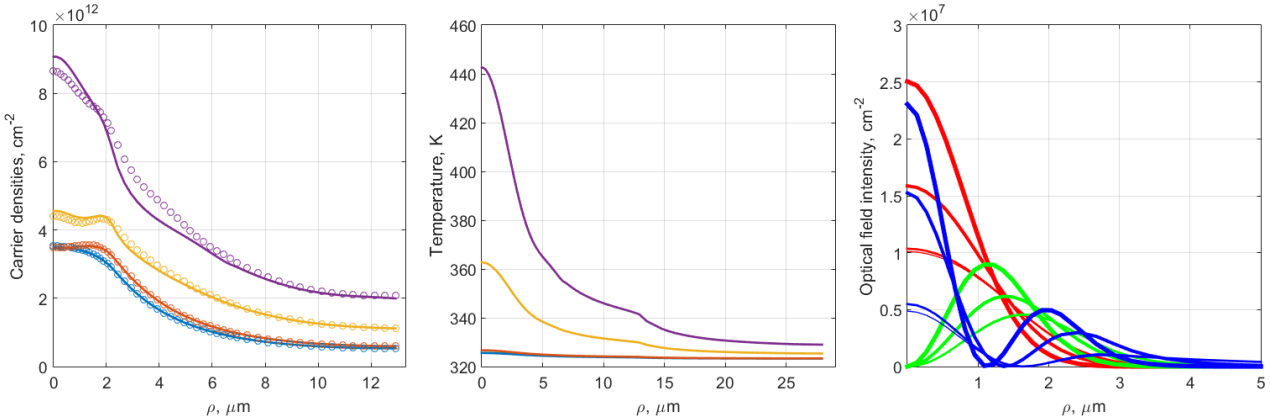

Figure 4. Internal parameters computed by VENUS at four different currents: 0.5, 1, 5, and 10 mA. From left to right: 2D electrons (continuous lines) and holes (open circles) in the central QW, related temperature profiles, and optical field intensity distributions for the three modes contributing to laser action. For this latter plot, the increase of current is rendered by thicker lines. Their colors refer to the three modes: LP_{01} (red), LP_{11} (green), LP_{02} (blue).

can be observed, namely from the weak guiding (provided by oxide aperture placed at a field antinode) at low pumping (thin curves) to the strong thermal lensing induced by the highest temperature profile shown in Fig. 4 center (10 mA injection, thick curves).

All these effects contribute actively to mode competition. Below threshold, carriers show a smooth bell-shaped profile centered on the device axis (blue curves in Fig. 4, left). As soon as lasing operation starts (1 mA, red curves), the optical field starts to dig a spatial hole into to 2D carriers, fostering the higher-order modes. In fact, they better overlap with the gain profile (directly related to the carrier profile) where they are maximum, *i.e.*, off-axis.

The interplay of these different and complex phenomena is synthesized in Fig. 5, where the modal gains and losses are reported versus current. When gain reaches a loss, the corresponding mode starts lasing. For small currents, modal losses decrease with current thanks to thermal lensing. However, for further increasing currents, the corresponding temperature rise leads to a gain shift and drop, which calls for higher carrier densities to compensate for the optical losses. Such carrier increase, which can be well appreciated in Fig. 4 (left), induces an

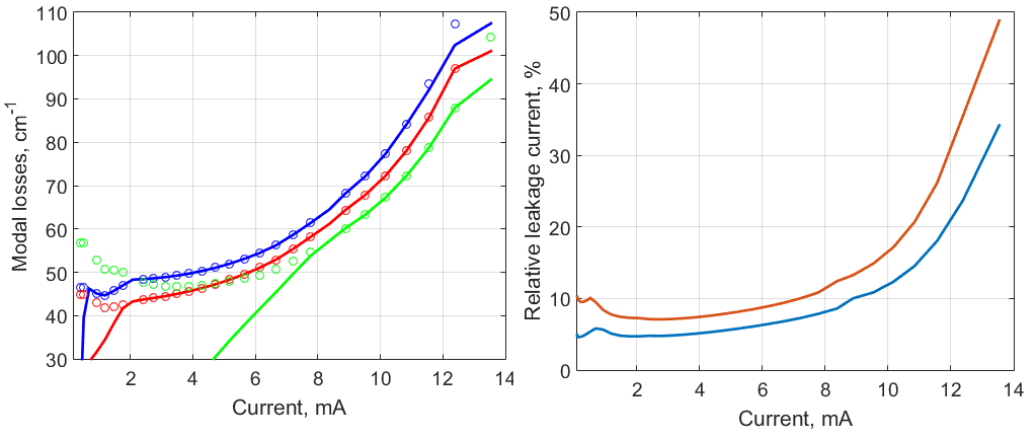

Figure 5. Left: modal gains (lines: blue LP_{01}, etc.) and compared to modal losses (VELM output, open circles) as a function of current. Right: current-dependent leakage current percentage. The red and blue lines refer to different ways of defining the leakage current. In blue we report the minority current at the edge of the 1λ-cavity (ideally it should be zero), in red the difference between the current and the integral of the capture term.[4]

Table 1. Transport, thermal and optical parameters of $Al_xGa_{1-x}As$.

Parameter	Values	Ref.	Parameter	Values	Ref.
χ_0, $x < 0.45$ (eV)	$4.07 - 1.1x$	31	μ_n, $x < 0.45$ ($cm^2/s/V$)	$(8 - 22x + 10x^2) \times 10^3$	31
χ_0, $x \geq 0.45$ (eV)	$3.64 - 0.14x$	31	μ_n, $x \geq 0.45$ ($cm^2/s/V$)	$-255 + 1160x - 720x^2$	31
$\varepsilon_{r,s}$	$12.90 - 2.84x$	31	$\mu_{p,300}$ ($cm^2/s/V$)	$370 - 970x + 740x^2$	31
$E_{g0,\Gamma}$ (eV)	$1.519 + 1.115x + 0.37x^2$	31	$\beta_{\mu,n}$	0.75	fit
$E_{g0,X}$ (eV)	$1.981 + 0.124x + 0.144x^2$	31	$\beta_{\mu,p}$	0.75	fit
$E_{g0,L}$ (eV)	$1.815 + 0.69x$	31	$\tau_{n,300}^{SRH}$ (ns)	1	fit
β_g (K)	204	31	$\tau_{p,300}^{SRH}$ (ns)	1	fit
α_Γ (eV/K)	5.41×10^{-4}	31	β_{SRH}	1	fit
α_X (eV/K)	4.6×10^{-4}	31	B^{rad} (cm^3/s)	1.8×10^{-10}	31
α_L (eV/K)	6.05×10^{-4}	31	C_n^{Aug} (cm^6/s)	5×10^{-31}	fit
α_χ (eV/K)	2.75×10^{-4}	31	C_p^{Aug} (cm^6/s)	3.75×10^{-31}	fit
ΔE_A		38	κ_{air} (W/m/K)	0.025	31
ΔE_D (eV)		38	κ_{cavity} (W/m/K)	7.8 (13)	fit
m_Γ/m_0	$0.067 + 0.083x$	39	$\kappa_{mirror,t}$ (W/m/K)	11.6 (14.5)	fit
m_X/m_0	$0.850 - 0.140x$	39	$\kappa_{mirror,z}$ (W/m/K)	9.3 (15.5)	fit
m_L/m_0	$0.560 + 0.100x$	39	$\kappa_{substrate}$ (W/m/K)	27.6 (46)	fit
m_p/m_0	$0.5 + 0.29x$	40	κ_{passiv} (W/m/K)	0.4 (0.5)	fit
$\tau_{scat,n}$ (ps)	10	fit	κ_{metal} (W/m/K)	300	31
$\tau_{scat,p}$ (ps)	5	fit	β_T	-1.30	32
n_{AlGaAs}		41	dn/dT (1/K)	2×10^{-4}	41

increase of free-carrier absorption, incrementing with temperature as well. Such an internal loss rise, together with the exponential growth of the leakage current, is responsible for the power rollover, and eventually for the switch-off of the device. In Fig. 5 (right) the leakage contribution to the total current is reported in percentage, emphasizing its detrimental effect. It is to be remarked that in previous works Auger recombination processes were identified as the fundamental mechanisms limiting lasing operation in VCSELs.[4,35–37] This is not in contradiction with the present discussion, since the different considerations can be ascribed to the peculiar surface relief design, which leads to large lasing threshold currents.

3. CONCLUSIONS

Vertical-cavity surface-emitting lasers represent a formidable challenge from a modeling perspective. In this work we unravel such a complex tangle by means of our in-house multiscale, multiphysical VCSEL electro-opto-thermal numerical simulator VENUS. After briefly recalling the main VENUS features and outputs, we demonstrate its validity through a comparison with experimental results. Then, the discussion focuses on some specific aspects of the multiphysical interplay ruling the transverse mode competition, whose correct reproduction demonstrates the VENUS potential to simulate any VCSEL concept in different operating conditions.

APPENDIX A. MATERIAL PARAMETERS OF $AL_XGA_{1-X}AS$

This appendix provides some details about the material parameters used in the simulations presented in this work.

The bandgap thermal dependence is modeled as

$$E_g = E_{g,0} - \alpha_g \frac{T^2}{\beta_g + T}. \tag{1}$$

Starting from this expression, the densities of states are evaluated by a many-valley description.[29]

The mobility dependence on doping impurity concentrations is described by a modified Hilsum model[33] calibrated on experimental values

$$\mu_{n/p,300} = \frac{\mu_{n/p,int}}{1 + \left(\frac{N_A + N_D}{N_X}\right)^{0.35}}, \tag{2}$$

where $\mu_{n/p,\mathrm{int}}$ indicates the mobility of the intrinsic material, N_D and N_A are the donor and acceptor doping concentrations, and N_X is a fitting parameter; in our simulations, $N_X = 4 \times 10^{17}\,\mathrm{cm}^{-3}$.

The thermal dependence of mobility is described by the following expression:

$$\mu_{n/p} = \mu_{n/p,300} \left(\frac{T}{300\,\mathrm{K}} \right)^{\beta_{\mu,n/p}} . \tag{3}$$

The SRH lifetimes exhibit a similar temperature dependence:

$$\tau_{n/p}^{\mathrm{SRH}} = \tau_{n/p,300} \left(\frac{T}{300\,\mathrm{K}} \right)^{\beta_{\mathrm{SRH}}} . \tag{4}$$

REFERENCES

[1] Michalzik, R., ed., [VCSELs: Fundamentals, Technology and Applications of Vertical-Cavity Surface-Emitting Lasers], Springer-Verlag, Berlin (2013).

[2] Moench, H., Carpaij, M., Gerlach, P., Gronenborn, S., Gudde, R., Hellmig, J., Kolb, J., and v.d. Lee, A., "VCSEL based sensors for distance and velocity," in [Proc. SPIE 9766], 97660A-1–16 (Mar. 2016).

[3] Ebeling, K. J., Michalzik, R., and Moench, H., "Vertical-cavity surface-emitting laser technology applications with focus on sensors and three-dimensional imaging," Japan. J. Appl. Phys. **52**, 08PA02-1–11 (2018).

[4] Tibaldi, A., Bertazzi, F., Goano, M., Michalzik, R., and Debernardi, P., "VENUS: a Vertical-cavity surface-emitting laser Electro-opto-thermal NUmerical Simulator," IEEE J. Select. Topics Quantum Electron. **25**(6), 1–12 (2019).

[5] Bava, G. P., Debernardi, P., and Fratta, L., "Three-dimensional model for vectorial fields in vertical-cavity surface-emitting lasers," Phys. Rev. A **63**(2), 23816-1–13 (2001).

[6] Debernardi, P. and Bava, G. P., "Coupled mode theory: a powerful tool for analyzing complex VCSELs and designing advanced devices features," IEEE J. Select. Topics Quantum Electron. **9**(3), 905–917 (2003).

[7] Bienstman, P., Baets, R., Vukusic, J., Larsson, A., Noble, M. J., Brunner, M., Gulden, K., Debernardi, P., Fratta, L., Bava, G. P., Wenzel, H., Klein, B., Conradi, O., Pregla, R., Riyopoulos, S. A., Seurin, J.-F. P., and Chuang, S. L., "Comparison of optical VCSEL models on the simulation of oxide-confined devices," IEEE J. Quantum Electron. **37**(12), 1618–1631 (2001).

[8] Debernardi, P., Bava, G. P., Degen, C., Fischer, I., and Elsäßer, W., "Influence of anisotropies on transverse modes in oxide-confined VCSELs," IEEE J. Quantum Electron. **38**(1), 73–84 (2002).

[9] Debernardi, P., Bava, G. P., Monti di Sopra, F., and Willemsen, M. B., "Features of vectorial modes in phase-coupled VCSEL arrays: experiments and theory," IEEE J. Quantum Electron. **39**(1), 109–119 (2003).

[10] Debernardi, P., Ostermann, J. M., Sondermann, M., Ackermann, T., Bava, G. P., and Michalzik, R., "Theoretical-experimental study of the vectorial modal properties of polarization-stable multimode grating VCSELs," IEEE J. Select. Topics Quantum Electron. **13**(5), 1340–1348 (2007).

[11] Debernardi, P., Orta, R., Gründl, T., and Amann, M.-C., "3-D vectorial optical model for high-contrast grating vertical-cavity surface-emitting lasers," IEEE J. Quantum Electron. **49**(2), 137–145 (2013).

[12] Tibaldi, A., Debernardi, P., and Orta, R., "High-contrast grating performance issues in tunable VCSELs," IEEE J. Quantum Electron. **51**(12), 2400407-1–8 (2015).

[13] Orta, R., Tibaldi, A., and Debernardi, P., "Bimodal resonance phenomena–part I: generalized Fabry–Pérot interferometers," IEEE J. Quantum Electron. **52**(12), 6100508-1–8 (2016).

[14] Tibaldi, A., Debernardi, P., and Orta, R., "Bimodal resonance phenomena–part III: high-contrast grating reflectors," IEEE J. Quantum Electron. **54**(6), 6600108-1–8 (2018).

[15] Debernardi, P., Tibaldi, A., Gerlach, P., Martelli, P., Boffi, P., Martinelli, M., Coviello, D., and Orta, R., "Modal performance of spiral phase plate VCSELs," IEEE J. Quantum Electron. **52**(5), 2400108-1–8 (2016).

[16] Bertazzi, F., Goano, M., Ghione, G., Tibaldi, A., Debernardi, P., and Bellotti, E., "Electron transport," in [Handbook of Optoelectronic Device Modeling and Simulation], Piprek, J., ed., ch. 2, 35–80, CRC Press, Boca Raton, FL (2017).

[17] Foreman, B. A., "Elimination of spurious solutions from eight-band $k \cdot p$ theory," Phys. Rev. B **56**, R12748–R12751 (Nov. 1997).

[18] Liu, G. and Chuang, S.-L., "Modeling of Sb-based type-II quantum cascade lasers," Phys. Rev. B **65**, 165220-1–10 (2002).

[19] Qiao, P.-F., Mou, S., and Chuang, S. L., "Electronic band structures and optical properties of type-II superlattice photodetectors with interfacial effect," Opt. Express **20**(2), 2319–2334 (2012).

[20] Zhou, X., Bertazzi, F., Goano, M., Ghione, G., and Bellotti, E., "Deriving $k \cdot p$ parameters from full-Brillouin-zone descriptions: A finite-element envelope function model for quantum-confined wurtzite nanostructures," J. Appl. Phys. **116**, 033709 (2014).

[21] Tibaldi, A., Orta, R., Peverini, O. A., Addamo, G., Virone, G., and Tascone, R., "Skew incidence plane-wave scattering from 2-D dielectric periodic structures: analysis by the mortar-element method," IEEE Trans. Microwave Theory Tech. **63**(1), 11–19 (2015).

[22] Selberherr, S., [Analysis and Simulation of Semiconductor Devices], Springer-Verlag, Wien (1984).

[23] Bertazzi, F., Cappelluti, F., Donati Guerrieri, S., Bonani, F., and Ghione, G., "Self-consistent coupled carrier transport full-wave EM analysis of semiconductor traveling-wave devices," IEEE Trans. Microwave Theory Tech. **54**, 1611–1618.

[24] Gioannini, M., Cédola, A. P., Di Santo, N., Bertazzi, F., and Cappelluti, F., "Simulation of quantum dot solar cells including carrier intersubband dynamics and transport," IEEE J. Photovoltaics **3**(4), 1271–1278 (2013).

[25] Witzigmann, B., Witzig, A., and Fichtner, W., "A multidimensional laser simulator for edge-emitters including quantum carrier capture," IEEE Trans. Electron Devices **47**, 1926–1934 (2000).

[26] Streiff, M., Witzig, A., Pfeiffer, M., Royo, P., and Fichtner, W., "A comprehensive VCSEL device simulator," IEEE J. Select. Topics Quantum Electron. **9**(3), 879–891 (2003).

[27] Goano, M., Bertazzi, F., Zhou, X., Mandurrino, M., Dominici, S., Vallone, M., Ghione, G., Tibaldi, A., Calciati, M., Debernardi, P., Dolcini, F., Rossi, F., Verzellesi, G., Meneghini, M., Trivellin, N., De Santi, C., Zanoni, E., and Bellotti, E., "Challenges towards the simulation of GaN-based LEDs beyond the semi-classical framework," in [SPIE Photonics West, Physics and Simulation of Optoelectronic Devices XXIV], Witzigmann, B., Osiński, M., and Arakawa, Y., eds., **Proc. SPIE 9742**, 974202-1–11 (Feb. 2016).

[28] De Santi, C., Meneghini, M., Tibaldi, A., Vallone, M., Goano, M., Bertazzi, F., Verzellesi, G., Meneghesso, G., and Zanoni, E., "Physical mechanisms limiting the performance and the reliability of GaN-based LEDs," in [Nitride Semiconductor Light-Emitting Diodes], Huang, J. J., Kuo, H. C., and Shen, S.-C., eds., ch. 14, 455–489, Woodhead Publishing, Duxford, U.K., 2nd ed. (2018).

[29] Calciati, M., Tibaldi, A., Bertazzi, F., Goano, M., and Debernardi, P., "Many-valley electron transport in AlGaAs VCSELs," Semiconductor Sci. Tech. **32**(5), 055007-1–6 (2017).

[30] Debernardi, P., Kroner, A., Rinaldi, F., and Michalzik, R., "Surface relief versus standard VCSELs: a comparison between experimental and hot-cavity model results," IEEE J. Select. Topics Quantum Electron. **15**(3), 828–837 (2009).

[31] Ioffe Physico-Technical Institute, St. Petersburg, Russia, "Physical properties of semiconductors," http://www.ioffe.ru/SVA/NSM/Semicond/index.html.

[32] Adachi, S., ed., [Properties of Aluminium Gallium Arsenide], EMIS Datareviews Series, INSPEC, London (1993).

[33] Hilsum, C., "Simple empirical relationship between mobility and carrier concentration," Electron. Lett. **10**(13), 259–260 (1974).

[34] Sakaki, H., Noda, T., Hirakawa, K., Tanaka, M., and Matsusue, T., "Interface roughness scattering in GaAs/AlAs quantum wells," Appl. Phys. Lett. **51**(23), 1934–1936 (1987).

[35] Bertazzi, F., Goano, M., and Bellotti, E., "Calculation of Auger lifetime in HgCdTe," J. Electron. Mater. **40**(8), 1663–1667 (2011).

[36] Calciati, M., Goano, M., Bertazzi, F., Vallone, M., Zhou, X., Ghione, G., Meneghini, M., Meneghesso, G., Zanoni, E., Bellotti, E., Verzellesi, G., Zhu, D., and Humphreys, C., "Correlating electroluminescence characterization and physics-based models of InGaN/GaN LEDs: pitfalls and open issues," AIP Adv. **4**, 067118-1–23 (2014).

[37] Bertazzi, F., Goano, M., Zhou, X., Calciati, M., Ghione, G., Matsubara, M., and Bellotti, E., "Looking for Auger signatures in III-nitride light emitters: a full-band Monte Carlo perspective," Appl. Phys. Lett. **106**, 061112-1–5 (Feb. 2015).

[38] Pavesi, L. and Guzzi, M., "Photoluminescence of $Al_xGa_{1-x}As$ alloys," J. Appl. Phys. **75**(10), 4779–4842 (1994).

[39] Adachi, S., "GaAs, AlAs, and $Al_xGa_{1-x}As$: Material parameters for use in research and device applications," J. Appl. Phys. **58**, R1–R29 (Aug. 1985).

[40] Chuang, S. L., [Physics of Photonic Devices], John Wiley & Sons, Hoboken (2009).

[41] Corzine, S. W., Design of vertical-cavity surface-emitting lasers with strained and unstrained quantum well active regions, PhD thesis, University of California, Santa Barbara (1993).